Earth and Planetary Science Letters 303 (2011) 1–10

Contents lists available at ScienceDirect

Earth and Planetary Science Letters

journal homepage: www.elsevier.com/locate/epsl

Metastable olivine wedge and deep dry cold slab beneath southwest Japan

Hitoshi Kawakatsu [a,*], Shoichi Yoshioka [b]

[a] Earthquake Research Institute, University of Tokyo, 1-1-1 Yayoi, Bunkyo-ku, Tokyo 113-0032, Japan
[b] Research Center for Urban Safety and Security, Organization of Advanced Science and Technology, Kobe University, 1-1 Rokkodai-cho, Nada-ku, Kobe 657-8501, Japan

ARTICLE INFO

Article history:
Received 4 October 2010
Received in revised form 8 January 2011
Accepted 12 January 2011
Available online 28 January 2011

Keywords:
metastable olivine
receiver function
slab
mantle transition zone
water transport

ABSTRACT

Oceanic plates subducted at trenches penetrate into the deep mantle, and encounter a structural boundary at a depth of 410 km where olivine, the dominant element of mantle rocks, transforms into a higher density form wadsleyite. This transformation may be delayed within the coldest core of subducting plates (slabs) due to kinetic effects, and it has been suggested that metastable olivine may persist deeper than 410 km. Using high density seismic array data in Japan, we show the direct image of the structure corresponding to this metastable olivine wedge (MOW) beneath southwest Japan. Numerical simulation of a subducting slab, including the kinetic effect of water (H_2O) on the olivine–wadsleyite transformation, indicates that the presence of the imaged MOW requires an insignificant amount of water (less than 100 wt. ppm) be present in the slab mantle, thus a deep dry cold slab. We infer that the transportation of water into the deep mantle occurs along the top surface of the subducting slab, but no significant amount within the slab itself. We also demonstrate that a numerical simulation including the kinetics of 660-km phase transformation can reconcile the observed deep depression of the 660-km discontinuity with a gentle Clapeyron slope.

1. Introduction

Water in the mantle is expected to play essential roles in various significant problems of geodynamics, and delineating its location and abundance in the mantle is considered as one of the most important issues in current solid geophysics (e.g., Karato, 2003). Recent seismological imaging of subduction zones with a dense network beneath northeastern Japan has successfully revealed how water may be transported into the mantle wedge of the subduction zone which might be responsible for arc volcanism (Kawakatsu and Watada, 2007; Tsuji et al., 2008). The results suggest that a significant amount of water is transported at least to depths of 130–150 km along the top surface of a subducting slab, observed as a low seismic velocity channel. As far as the global material circulations in the mantle are concerned, however, essential questions remain as to how deep this channel continues and how much water is present in the mantle part of the slab that may also carry water into the deeper mantle (Iwamori and Albaréde, 2008; Maruyama and Okamoto, 2007).

By reviewing the past literatures on the study of the top surface of the subducting Pacific plate beneath the Japanese islands (Fukao et al., 1978; Helffrich and Stein, 1993; Okada, 1979), Kawakatsu and Watada (2007) suggested that the aforementioned low velocity channel might continue deeper. Indeed Tonegawa et al. (2008) showed that such a LV channel was likely to exist beneath southwest Japan. Here by extending the high-resolution imaging of subducting Pacific slab deeper, we show that such a structure is likely to be present down to a depth of ~350 km beneath southwest Japan. Further we present a direct imaging of the postulated metastable olivine wedge (MOW) (Iidaka and Suetsugu, 1992; Sung and Burns, 1976; Wiens et al., 1993); together with a numerical simulation of the subducting slab, we infer that an insignificant amount of water is present in the slab mantle, thus a deep dry cold slab beneath southwest Japan, and that the transportation of water into the deep mantle likely to occur along the top surface of the subducting slab, but no significant amount within the slab itself.

2. Receiver function imaging beneath SW Japan

The receiver function (RF) technique (e.g., Ammon, 1991; Langston, 1979; Vinnik, 1977) has been a powerful tool to delineate fine structures in the subduction zones, and the fate of water initially trapped in the subducting oceanic crust has been extensively discussed (e.g., Abers, 2000; Bostock et al., 2002; Ferris et al., 2003; Yuan et al., 2000). The high density and high quality seismic networks in Japan have provided excellent opportunities to finely image the subducting slabs beneath Japan (e.g., Li et al., 2000; Niu et al., 2005; Ramesh et al., 2005; Shiomi et al., 2004; Tonegawa et al., 2008). The applicability of the short-period but high-density Hi-net data to image deep structures such as 410 km and 660 km discontinuities has been also demonstrated (Niu et al., 2005; Ramesh et al., 2005). Combining RF images properly accounted for the effect of the dipping structure, seismic tomography, and seismicity, Kawakatsu and Watada (2007) showed how water may be transported into the mantle wedge.

* Corresponding author. Tel.: +81 3 5841 5817; fax: +81 3 3812 9417.
E-mail address: hitosi@eri.u-tokyo.ac.jp (H. Kawakatsu).

0012-821X/$ – see front matter © 2011 Elsevier B.V. All rights reserved.
doi:10.1016/j.epsl.2011.01.008

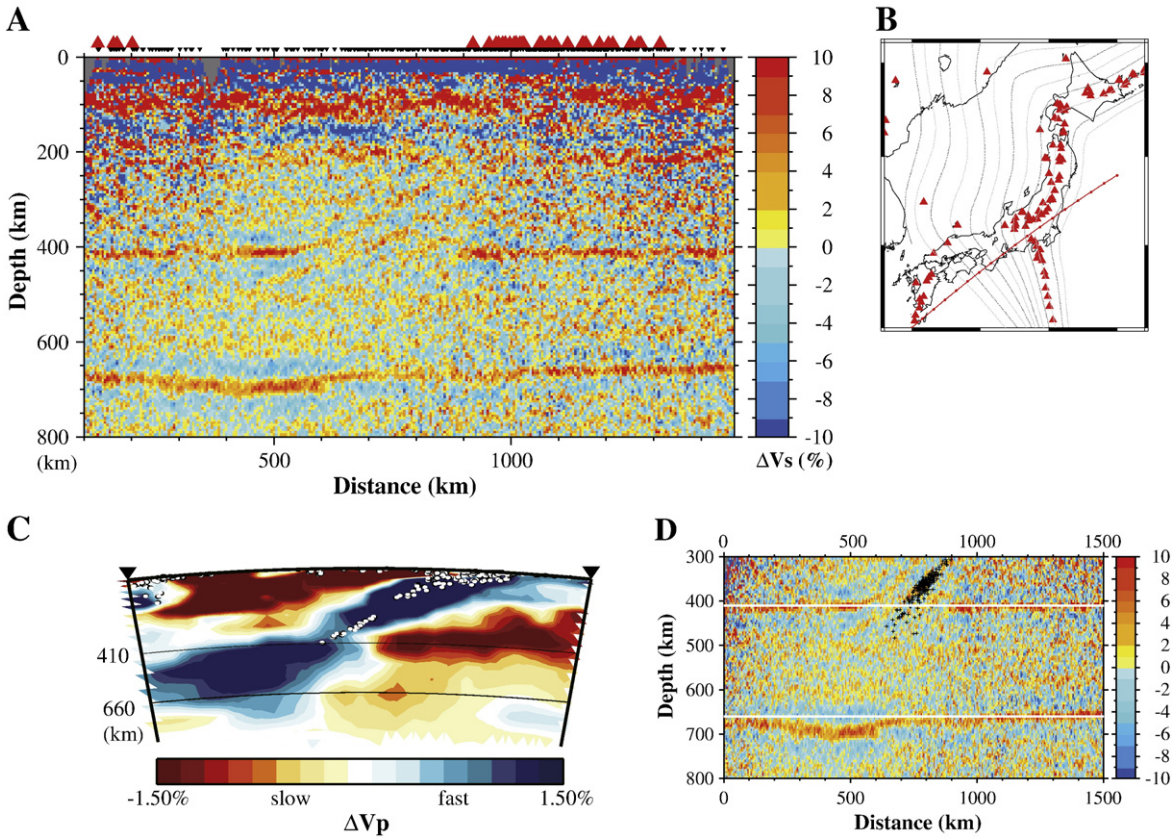

Fig. 1. The reflectivity profile beneath southwest Japan. (A) Reflectivities given by RFs are measures of local S-wave velocity jumps, as a P-to-S seismic wave conversion is sensitive to the S-wave velocity change. RFs are averaged over 3 degree-wide range along the red line in (B). Red and blue colors correspond to velocity increase and decrease with depth, respectively. Red triangles and reversed black triangles plotted on the top respectively indicate active volcanoes and stations used for the imaging located within the cross-section range. The color scale is given in terms of an equivalent S-wave velocity change at a first-order discontinuity in percent, but only relative values are meaningful. (B) A map of Japan with volcanoes (red triangles). Gray lines are isodepth contours (50 km–600 km) of the subducting Pacific slab (Gudmundsson and Sambridge, 1998). Distances in Figs. 1, 3, 4, 6, and 8 are measured from the southwest end point (30°N, 130°E) of the red line, and dots on the red lines are given in a 100 km interval. (C) Image of a global seismic tomography along the same cross section (Obayashi et al., 2009). (D) Enlarged section of (A) with vertical exaggeration. Two white horizontal lines are drawn at depths of 410 km and 660 km. Note the depression of 660 km discontinuity over about a 500 km width range. Plus marks indicate seismicity.

Fig. 1A shows the result of the conventional RF method as employed in Kawakatsu and Watada (2007) to image the whole of the Japanese subduction zone down to a depth of 800 km using the data described below. The section is chosen to be nearly parallel to the slab dip below ~400 km depth (Fig. 1B). Both the 410 km and 660 km discontinuities as well as a dipping signature corresponding to the top surface of the Pacific slab are imaged. Furthermore, the depression of the 660 km discontinuity is observed where the cold subducting Pacific slab is approaching the discontinuity that is generally understood as due to the negative Clapeyron slope for the ring-woodite to perovskite (Pv) plus magnetiowüstite (Mw) phase transformation (Bina and Helffrich, 1994). Beneath southwest Japan, where the ray coverage of our imaging for the mantle transition zone (MTZ) is the best, the 660 km discontinuity appears to be deflected downwards as much as ~40 km over a width of approximately 500 km (Fig. 1D). This is the region where the Pacific plate appears to stagnate in the MTZ in recent tomographic models (Fig. 1C; Fukao et al., 2009). The observed width of the depression of the 660 km discontinuity appears to be consistent neither with a simple penetrating slab, nor with a flat stagnating slab above the boundary; in the former case, the depression width should be about 200 km, and in the latter case, the large depression of ~40 km is difficult to achieve. A more complex slab morphology and/or nature of the phase boundary in the MTZ may be required to explain the observation (Bina and Kawakatsu, 2010; Niu et al., 2005).

A signature corresponding to the low-velocity channel atop the slab may be traced as deep as ~350 km (dipping nearly continuous red images in Fig. 1), suggesting at least some of the water transported into mantle wedge in shallower range (Kawakatsu and Watada, 2007) may be transported to this depth. This is consistent with a view that this portion of the subducting Pacific slab is relatively cold due to the presence of the Philippine Sea slab in the mantle wedge at shallow depth, and the water can be transported deeper along the top surface of the subducting plate (Iwamori, 2007).

2.1. Vectorial receiver function imaging

To image the subducting Pacific plate better, we have extended the treatment of Kawakatsu and Watada (2007), in which they corrected for the effect of a dipping interface on seismic receiver functions, by introducing a *vectorial receiver function* (VRF) method (Kawakatsu, 2008; Kawakatsu et al., 2009). When a conversion plane is dipping, a P-to-S converted wave of a RF can have components both in radial and transverse directions of the incoming teleseismic P-wave (Fig. 2A). So if we know that the structure responsible for conversion may be dipping as in the case of the subduction zone, we may rotate radial and transverse RFs into the expected direction component of the P-to-S converted wave to use for the imaging of the dipping interface. This is essentially the same as for the conventional RF imaging that assumes a horizontally stratified structure.

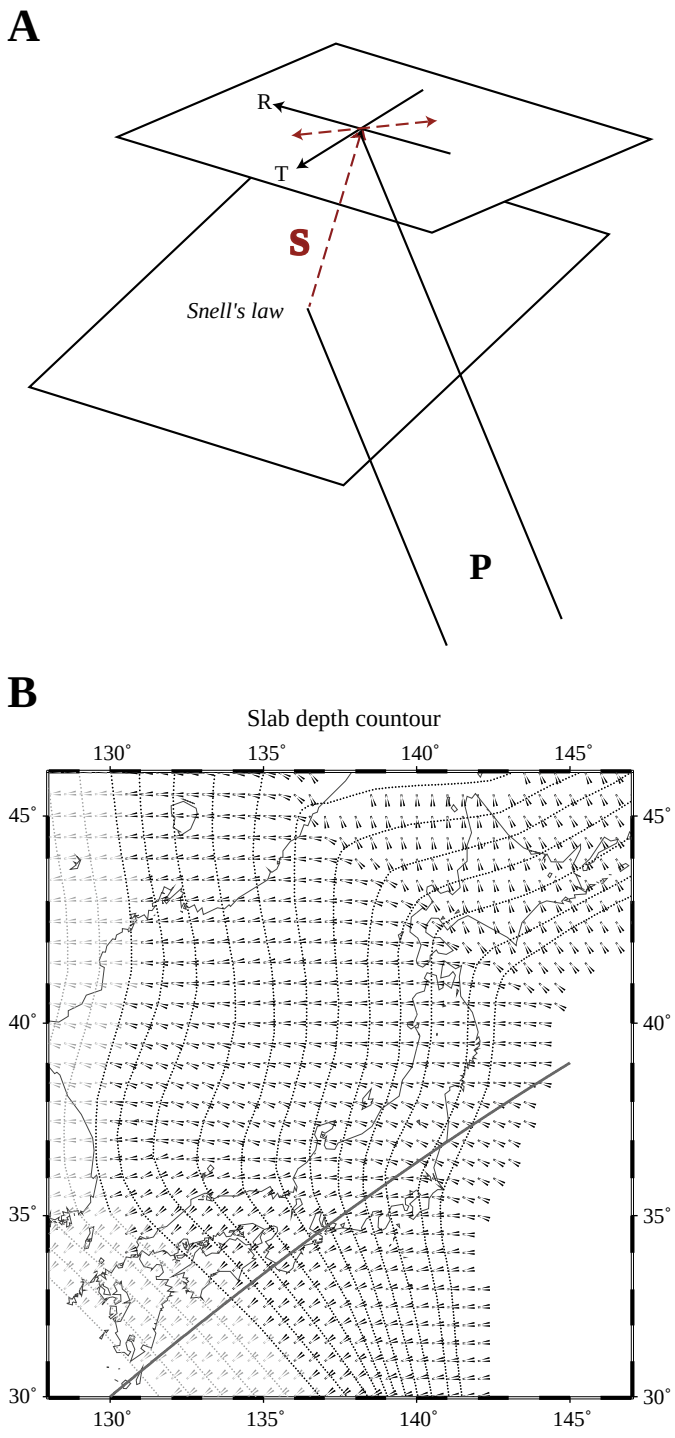

Fig. 2. (A) A schematic figure showing the VRF ray geometry. P-rays are represented by black solid lines and S-rays by red broken lines. (B) Depth contours of the subducting Pacific slab employed for the VRF imaging. Iso-depth contours are given with a 50 km interval from 50 km to 800 km. Black dots are those from (Gudmundsson and Sambridge, 1998) derived from seismicity and used for the VRF imaging in Figs. 3, 6, and 8. Gray dots are those estimated as a continuation of shallow ones and used for Fig. 4. From these contours, local dip angles and azimuth directions are estimated by a linear interpolation for every 0.1° both in latitude and longitude. Arrows indicate representative azimuth directions for every 0.5°. The back line denotes the section along which images are shown.

We employ the depth contour of the Pacific plate estimated from seismicity (Gudmundsson and Sambridge, 1998) to correct the effect of the dipping interface (Fig. 2B). For each segment of a RF waveform, the potential conversion point for the assumed 1D reference structure (IASP91; Kennett and Engdahl, 1991) is first determined as done for the conventional CCP (common conversion point) stacking. If the conversion point depth is larger than 40 km, the estimated latitude and longitude are used to obtain the local dip of the Pacific slab (when there exists a slab right beneath or above) which is further used to locate the corresponding dipping conversion point. Among the potential P-to-S scattering points that give the same delay time (rays are traced assuming the same 1D IASP91 model for both P and S legs), only a P–S conversion which satisfies the Snell's law on an interface that dips parallel (within 0.6°) to the estimated local Pacific slab dip is used for the CCP stacking. (As this new conversion point is offset from the original one that is used to estimate the local dip, a new local dip can be re-estimated at the location of the new conversion point to iteratively solve for an updated dipping conversion point until convergence. The results, however, usually make no significant difference, and thus we only perform the first iteration.) Two horizontal component RFs are then rotated to the direction of expected polarization of P–S converted waves from the interface, and stacked at the conversion point in such a way that the amplitude corresponds to the possible S-wave velocity jump at the interface. (When the expected conversion coefficient (P-to-S) is so small that makes this estimation of the S-wave velocity jump unstable, we provide some minimum threshold value for the conversion coefficient.)

This CCP stacking method for a dipping interface is applied to Hi-net recording of teleseismic events from 2001 to the end of 2006. We select those in a distant range of 30–90° with M_w>5.5. The total number of events analyzed is 681, and the number of RFs is more than 300,000. RFs are constructed for instrument response corrected seismograms employing the water level correction (C = 0.001) (Ammon, 1991) in a frequency range of 0.1–0.5 Hz as done in our earlier work (Kawakatsu and Watada, 2007). RFs are migrated into space-domain and summed for each 5 km × 5 km block. The VRF correction is applied for images below a depth of 40 km, and the images above the depth is meaningless because of the sign convention employed in plotting. Besides the image of the MOW presented here, a clear image of a bottom boundary of the subducting Pacific plate has been successfully obtained (Kawakatsu et al., 2009).

2.2. Direct imaging of MOW

Besides the aforementioned well known features of the subducting slab (Fig. 1), the vectorial RF images show additional features (Fig. 3); below 350 km right beneath southwest Japan, there exist two signatures with opposite signs parallel to each other and also to the dipping slab (Fig. 3A–B). Comparison with the catalogue seismicity by Japan Meteorological Agency (JMA) (Fig. 3D) and a regional tomographic image (Matsubara et al., 2008, Fig. 3C) indicates that these signatures occur inside of the Pacific slab (note that deep earthquakes are located about 40 km away from the top surface of the slab and near the lower-red one of the two signatures.) Considering that the upper (blue) signature corresponds to a velocity decrease (from shallow to deep) and the lower (red) one to a velocity increase, the image indicates that there is a low velocity layer surrounded by sharp boundaries within the slab at depth between depths of ~350 km and 450 km. An upward continuation of the red (slightly blurred) image appears to extend to a depth of ~300 km or even shallower in Fig. 3A, but this signature appears to be originated from rays of limited back-azimuth ranges (see Discussion).

Fig. 4 shows similar VRF images for a case that the Pacific slab continues to subduct deeper beyond seismicity (Fig. 2B). Fig. 4B shows the same section as Fig. 3A, while Figs. 4A and 4C correspond to one degree north and south of the section, respectively. Paired blue-red signatures are consistently observed in these images, indicating these are robust features of the imaging. On the other hand, the appearance of the upward continuation of the red image varies from south to north, suggesting that this does not correspond to a simple

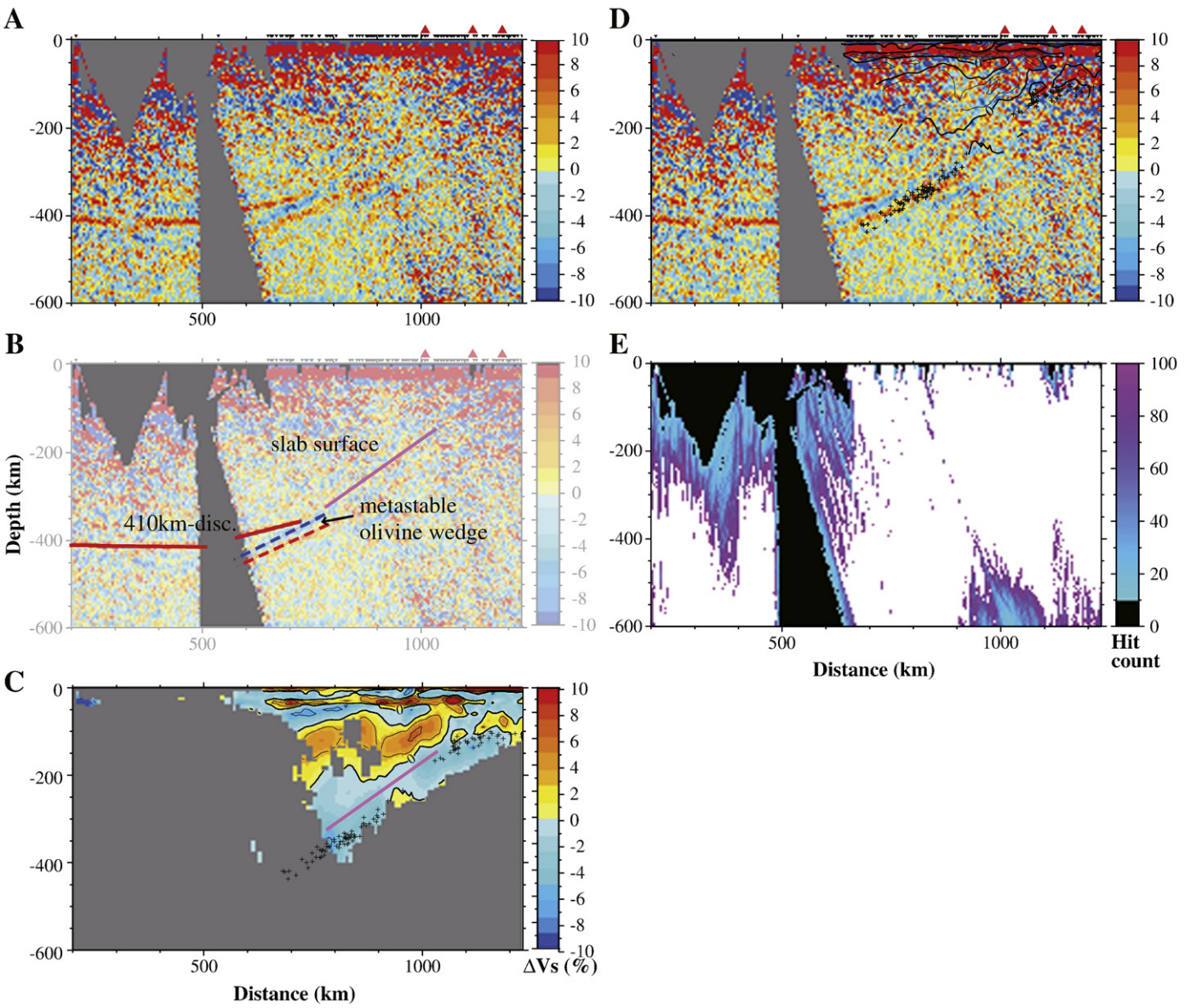

Fig. 3. Images of the metastable olivine wedge. (A) Vectorial RF image along the same profile with Fig. 1 (but for 1 degree-wide average, with reduced depth and distance ranges). In this particular profile, the dipping correction is applied for a horizontal distance range exceeding ~500 km where the seismicity indicates the presence of the slab. (B) Interpretation of the image is overlaid on top. The pink line indicates the slab top surface seen in Fig. 6. Two red lines indicate flat and elevated 410 km discontinuities. Blue and red broken lines denote upper and lower surfaces of the MOW. (C) Image of a regional S-wave tomography (Matsubara et al., 2008) with seismicity. (D) Same as (A) with seismicity. (E) Ray coverage of receiver functions. RFs are those averaged for every 5 km-square block. No smoothing is applied for all the images shown in this paper. The number of rays are counted for each block and shown. Those boxes with more than a hundred hits are shown by white.

structure parallel or subparallel to the slab dip. We thus suggest that the low velocity layer exists only below ~350 km depth. Fig. 4 also shows that the 410 km discontinuity is lifted upward (also toward the slab) as a result of the dip correction.

The most natural explanation for the low velocity layer within the deep slab seems to attribute it to the presence of the postulated metastable olivine wedge (Sung and Burns, 1976). Indeed this is the exact region where Iidaka and Suetsugu (1992) inferred such a presence from the travel time analysis, and also such low velocity layers are reported elsewhere (Jiang et al., 2008; Kaneshima et al., 2007). Bina and Kawakatsu (2010) recently showed that, by calculating the gradient of bulk sound velocity predicted for the appropriate subduction condition beneath Japan, the nearly isothermal and essentially univariant boundaries of a MOW were potentially more reflective than either of the main transition zone seismic discontinuities (Fig. 5), supporting our interpretation. We thus conclude that the first direct imaging for the MOW is obtained.

Fig. 6 compares the image obtained by VRF with those of radial and transverse component-only RF images (RRF and TRF, respectively). In the radial image with dip correction, the top surface of the slab (indicated by a while line) is seen between depths of 200 km and 350 km. Also the signatures corresponding to MOW are emerged around a point of 400 km-depth and 700 km-horizontal distance. These MOW signatures are very strong in the transverse image. In the vectorial image, which is more or less an average of above two images, the MOW signatures are imaged strong, while the signature of the slab surface is somewhat reduced. Considering that ray coverage is much better to south, different ways that these dipping signatures appear in three images may be due to the difference of fabrics (i.e., anisotropy) causing them. For example, Tono et al. (2009) showed that a strong and consistent seismic anisotropy exists throughout the subducting Pacific slab beyond a depth of 400 km, and suggested a possible relation to the presence of the MOW (*cf.* Chen and Brudzinski, 2003). Our results may be consistent

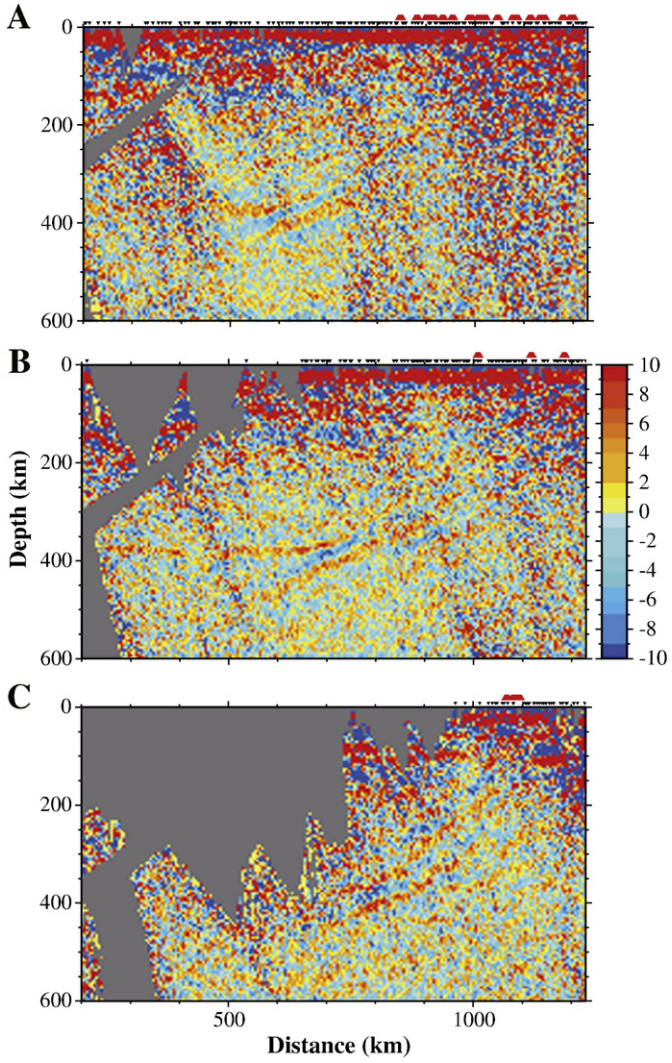

Fig. 4. VRF images in case of a deep continuous slab. The Pacific slab is assumed to subduct continuously down to 800 km as shown in gray dots in Fig. 2B. (A) A section 1-degree north of the section in (B). (B) VRF image along the same profile with Figs. 3 and 6 (1 degree-wide). The dipping correction is applied for the entire section. (C) A section 1-degree south of the section in (B).

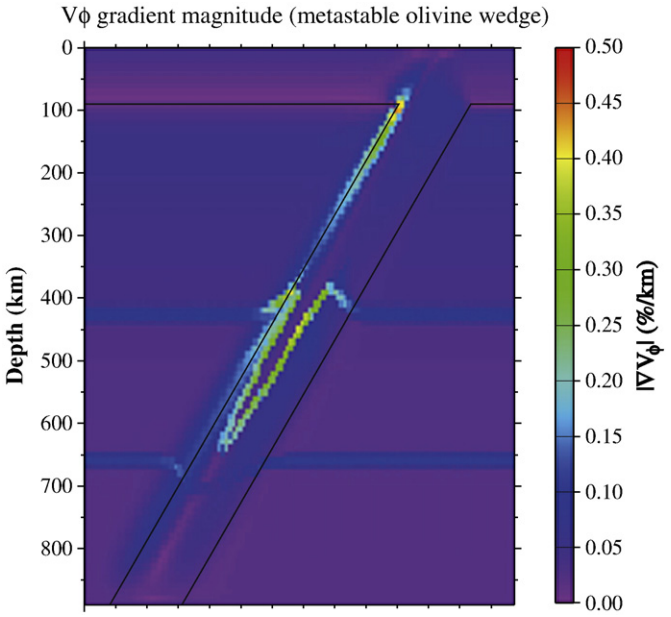

Fig. 5. Calculated magnitudes of bulk-sound velocity gradients for MOW. Note that nearly isothermal and essentially univariant boundaries of MOW are potentially more reflective than mantle transition zone seismic discontinuities. After Fig. 8 of Bina and Kawakatsu (2010). This model does not contain a petrologically distinct oceanic crustal layer, and the whole space is simply modeled as mantle composition.

with their observation, but further confirmation is needed that is left for the future work. We also note that the MOW signatures are imaged consistently using rays coming either from the Pacific side of the slab (back azimuth smaller than ~150°), or from the other side (more in Discussion).

3. Numerical modeling of the effect of H_2O on the kinetics associated with the olivine to wadsleyite phase transformation

Recent studies of high pressure and high temperature (high P–T) experiments indicate that metastable olivine might persist in a cold core of a slab due to the low rate of reaction associated with the olivine to wadsleyite phase transformation, and that the reaction is expected to be accelerated or decelerated depending on the amount of water present in the slab mantle (Kubo et al., 2002). The existence of the MOW imaged in this study, therefore, can be used to constrain the water content within the subducting slab mantle. To consider a problem of such non-equilibrium phase transformations, we developed a 2D Cartesian numerical code which incorporates the effect of kinetics of phase transformations into the conventional model of thermal convection which solves the momentum and energy equations simultaneously (Yoshioka et al., 2008; Yoshioka et al., in preparation). We consider kinetics of nucleation (Rubie and Ross, 1994) and growth of grains for the olivine to wadsleyite phase transformation (Hosoya et al., 2005) and also for the dissociation of ringwoodite to Pv + Mw (Kubo et al., 2002) which is responsible for the 660 km discontinuity. The effect of water content on the kinetics of the olivine–wadsleyite phase transformation within the slab as well as the latent heat release associated with a non-equilibrium phase transformation is taken into account. The solution of the energy equation is obtained self-consistently together with the solution of the equations of kinetics using the 4th-order Runge–Kutta method. Results of numerical simulation for a variety of subduction parameters show that the maximum depth of the MOW increases strongly with the thermal parameter of the slab (vertical subduction velocity times slab age), and decreases with the water content within the slab (Marton et al., 2005). The effects of latent heat release become more important with increasing depth of the phase transformation, leading to a temperature increase of more than 100 K at a depth of about 600 km. This temperature increase due to the latent heat release stimulates strongly further phase transformation, which plays an important role in accelerating the phase transformation, yielding a MOW with shorter length (Daessler and Yuen, 1996).

Fig. 7 shows temperature fields for a set of numerical simulation conducted using a particular set of subduction parameters for the slab beneath southwest Japan of this study (subduction velocity = 8 cm/yr, slab age = 150 My). The shape of the slab and other parameters are constrained from the RF images, seismicity and seismic tomography (Obayashi et al., 2009). The results appear to be consistent with the observed image of the MOW, and the water content in the deep part of the slab mantle here cannot exceed 100 wt. ppm. Otherwise, the metastable olivine does not survive deep enough. Considering the uncertainty of the assumed parameters, we estimate the upper bounds would be few hundreds wt. ppm, similar to a value reported in Mariana (Kubo et al., 2009). Our results indicate insignificant amount of water present in the subducting slab mantle in the studied region, thus a deep dry cold slab.

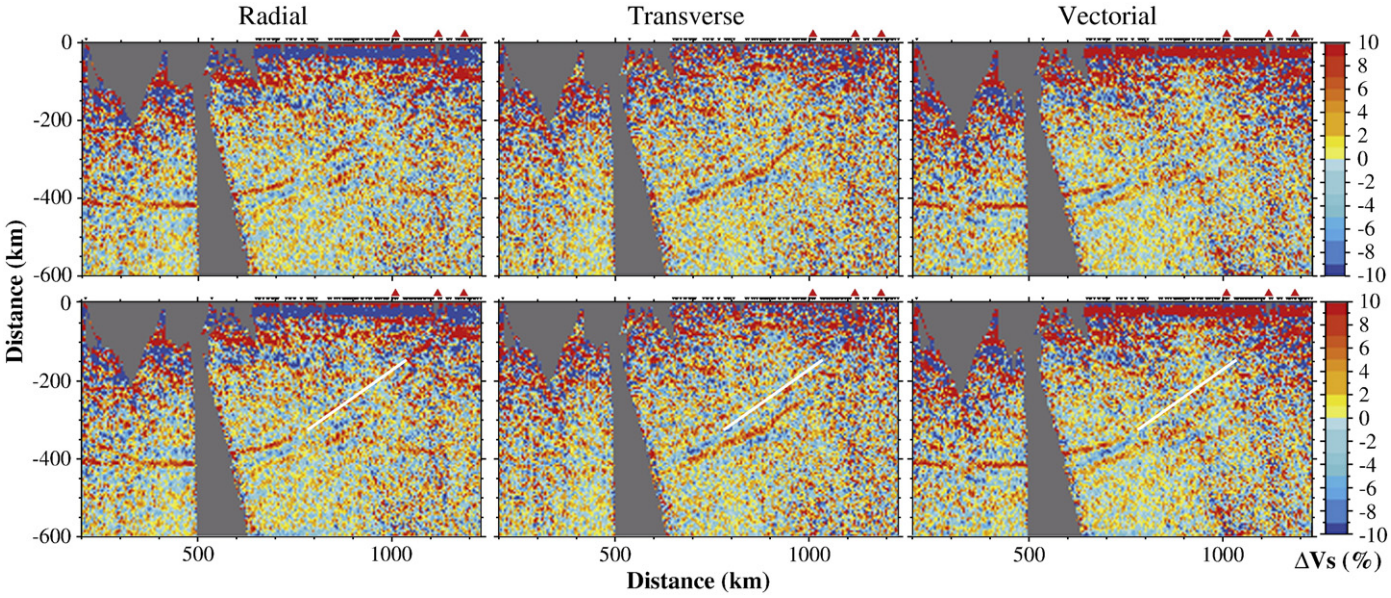

Fig. 6. Comparison of the vectorial RF image with single-component images for the same profile as in Fig. 3. Images in the second row are same as those in the first one except the white line indicating the top slab surface interpreted from the radial image.

4. Discussion

4.1. Effect of the uneven event distribution

The effect of the uneven event distribution is examined in Fig. 8, where individual rays are binned according to the back-azimuth at the conversion points. For every 15° range of the back-azimuth, rays are grouped. When the number of rays in each bin (n) exceeds a specified number (n_b), rays are weighted less by n_b/n as if there are only n_b rays. $n_b = 1$ corresponds to a case that bin averages are used for imaging, and $n_b \geq \max(n)$ corresponds to a case that each ray is weighted equally (i.e., no back-azimuth weighting). Fig. 8 shows images for $n_b = 3, 5, 10, \max(n)$. While the postulated MOW image of the present paper (Fig. 3) is stable, its apparent continuation above a depth of ~350 km degrades when back-azimuth weighting is employed, indicating that this particular image is strongly affected by rays from heavily concentrated certain directions. This situation can be further seen in Fig. 6. Both radial and transverse images show red signatures in the updip of the postulated MOW. A careful examination of these signatures, however, shows that they do not overlap each other when overlaid and when analyzed together as VRF, they do not interfere constructively (The signatures corresponding to MOW interfere constructively on the other hand.). This suggests that the updip images originate from a structure not in the plane subparallel to the subducting slab. They may be originated from the reported slab tear (Obayashi et al., 2009) or a related structure located outside of this studied region. We, however, note that the seismicity shows a continuous distribution of deep earthquakes from south (Izu–Bonin deep seismic zone) to the studied region without any apparent gap, and thus the suggested slab tear may not be affecting much the MOW in the studied region.

4.2. Sensitivity test of the numerical model

We performed sensitivity tests for some affecting parameters on our calculated results such as the age of the oceanic plate at the trench, the activation volume, the activation enthalpy, and the exponent of water content, by giving errors of ±5% for used values in this study. As a result, we found that water content of approximately 130 wt. ppm was the maximum to obtain the same depth of the tip of the MOW shown in Fig. 3, and that the exponent of water content affected mostly the results among the tested parameters. This indicates that dry slab model is preferable within the range of the assumed errors. In a series of this sensitivity test, we did not evaluate the effect of intra-grain nucleation which might occur at a depth of around 500 km. This is because this effect accelerates the reaction of the phase transformation, requiring smaller water content than 100 wt. ppm.

4.3. Modeling the kinetics of the 660-km phase transformation associated with a dry cold slab subduction

Recent high P–T experiments also suggest that the Clapeyron slope associated with the dissociation of ringwoodite to Pv + Mw under dry condition is quite gentle and about −1 MPa/K (Fei et al., 2004; Katsura et al., 2003). If we assume a value of −1.3 MPa/K, a temperature difference of 700°C between surrounding mantle and the coldest core of the slab at a depth of 660 km could contribute to the depression of the 660 km discontinuity to only 25 km. It is, therefore, hard to explain the observed depression of ~40 km for the 660-km discontinuity solely by direct thermal effect. However, the rest amount of depression of about 15 km is explainable by taking the kinetics of the 660-km phase transformation into account (Fig. 9) as recently advocated by Kubo et al. (2009). Our numerical simulation, which fully incorporates the kinetic effects of the phase transitions for both 410 km and 660 km discontinuities, is capable of modeling observed seismic features associated with the phase transformations for the deep dry cold slab beneath southwest Japan in a self-consistent manner (Fig. 10A).

4.4. Seismic constraints on the deep water transportation beneath SW Japan

Based on the RF analysis of the Hi-net tiltmeter recordings (can be considered as long-period seismograms), Tonegawa et al. (2008) suggested that the low velocity channel above the Pacific slab might continue down to ~500 km, indicating the transportation of water into the mantle transition zone. Their interpretation is, however, based on a dipping signature that is considered as the top of the subducting slab. With an appropriate dip correction for the imaging, this dipping structure coincides with the lower edge of the MOW imaged in the present paper, and thus their interpretation is likely to be mistaken (T. Tonegawa, 2010, personal communication). With the

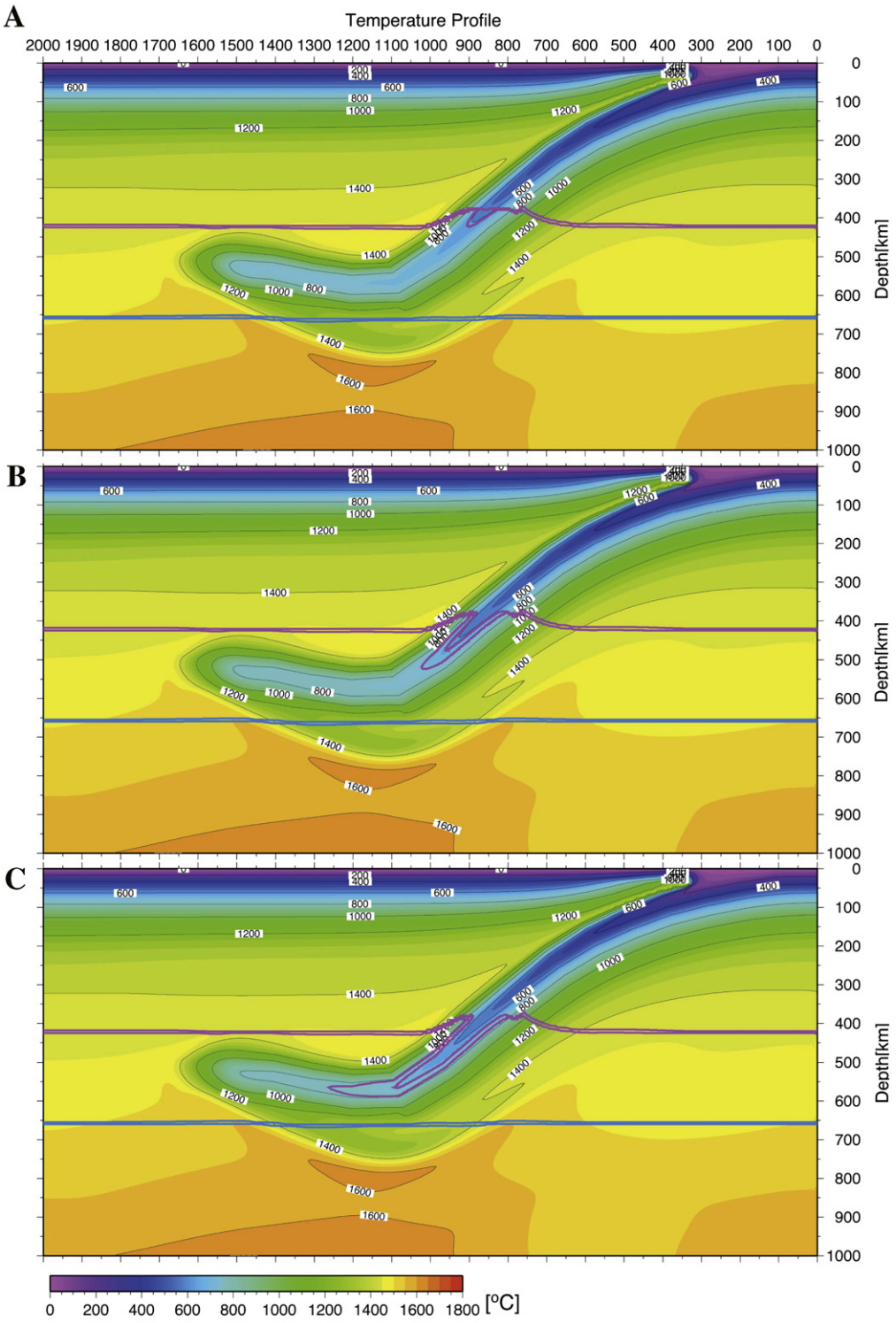

Fig. 7. Kinetic effect of water on the 410 km-phase transition. Temperature distributions associated with subduction of the Pacific plate in a vertical cross section along the profile in Fig. 1B at 20 Myr since the initiation of subduction. (The 20 Myr period is chosen to be consistent with the seismologically observed geometry (length) of the stagnant slab, but using longer durations of subduction does not alter the appearance of the MOW significantly.) Subduction velocity of 8 cm/yr, the age of the oceanic plate at a trench of 150 Myr, and the Clapeyron slope associated with the phase transformation from ringwoodite to Pv + Mw of −1 MPa/K are assumed. The two pink lines denote the lines representing 10% (the shallower line) and 90% (the deeper line) completion of the phase transformation from olivine to wadsleyite, whereas the two blue lines represent 10% and 90% completion of the phase transformation from ringwoodite to Pv + Mw. Water content is (A) 300 wt. ppm, (B) 100 wt. ppm, and (C) 50 wt. ppm. Note that with more than 300 wt. ppm of water, the MOW should not be present.

available seismological data so far, we can only trace the low velocity channel that may correspond to the pathway of water into the deep mantle down to ~350 km beneath SW Japan.

The apparently seamless continuation of the top of slab ending ~350 km depth (interpreted to be the base of a hydrous low velocity layer) with the upward sloping limb of the 410 km discontinuity on

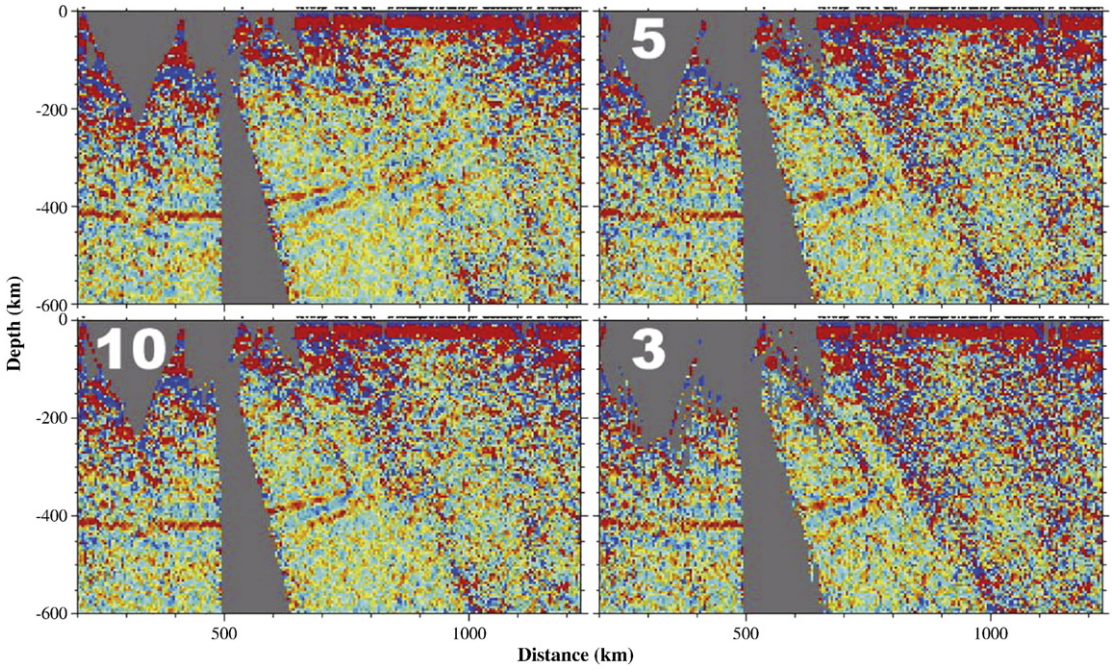

Fig. 8. Effect of back-azimuth weighting. The upper-left panel shows the same image as Fig. 3A. For the rest, the number at upper-left corner of each panel gives the ray number threshold, n_b used for weighting.

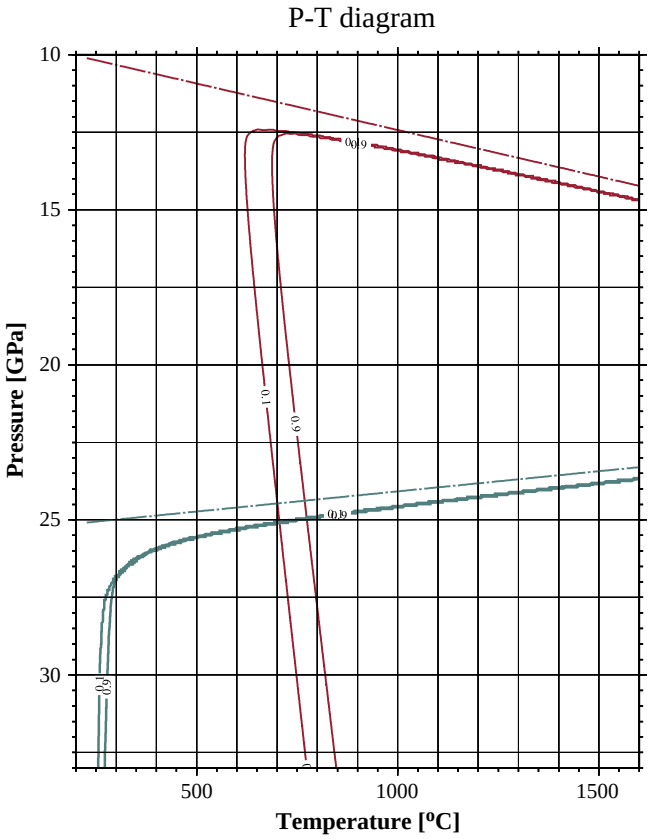

Fig. 9. Phase diagram on P–T space showing the phase transformations from olivine to wadsleyite (red lines) and from ringwoodite to Pv + Mw (peacock-green lines). The dash-dotted and solid lines denote equilibrium boundary and non-equilibrium boundary due to kinetics (10% and 90% completion of transformation), respectively. The assumed values of the Clapeyron slope for the ringwoodite to Pv + Mw phase transformation, subduction velocity and water content are −1.3 MPa/K, 8 cm/yr, and 100 wt. ppm, respectively.

the landward side of subduction (Fig. 3A) poses an interesting question regarding on the fate of water down at the depth range. Although the theoretical calculation of Bina and Kawakatsu (2010) for anhydrous mantle shown in Fig. 5 predicts that the upward sloping limb of the 410 km discontinuity can be quite visible seismically, the seamless continuation of two signatures may indicate that the hydrous layer merges into the postulated silicate melt layer atop of the 410 km discontinuity first suggested by Revenaugh and Sipkin (1994). We, however, do not observe a signature corresponding to the top of the low-velocity melt layer (should be seen as a blue image around a 300 km–350 km depth range) that has been reported elsewhere (e.g., Revenaugh and Sipkin, 1994; Schaeffer and Bostock, 2010; Tauzin et al., 2010). This may indicate that the top of the low-velocity melt layer is a gradual boundary in this studied region that cannot be well imaged in the frequency range of our dataset. The situation is, however, similar for the results using longer-period data (Tonegawa et al., 2008), leaving also a question for such a presence in this region.

Fig. 10B summarizes our findings. Together with the existing simulation for the water transportation in cold subduction environment (Iwamori, 2007; Tonegawa et al., 2008), we infer that water is transported into the deep mantle mainly along the top surface of the subducting slab, but no significant amount by the slab itself. This suggestion appears contrary to the generally accepted view that intermediate depth earthquakes are caused by dehydration embrittlement (Peacock, 2001) that requires the presence of water in the slab, but is more consistent with a mechanism such as recently advocated by Kelemen and Hirth (2007) that does not require water. Reynard et al. (2010) recently suggested that the slow P-wave speed in the lower-plane of the double seismic zone might not require the presence of water inside the slab mantle in the intermediate depth range.

Acknowledgements

We thank the Hi-net data center for providing us with the high quality waveform data, and M. Obayashi for their most-updated tomography model. SY thanks Y. Torii and T. Kubo for their kind help on the numerical simulation of the temperature calculation.

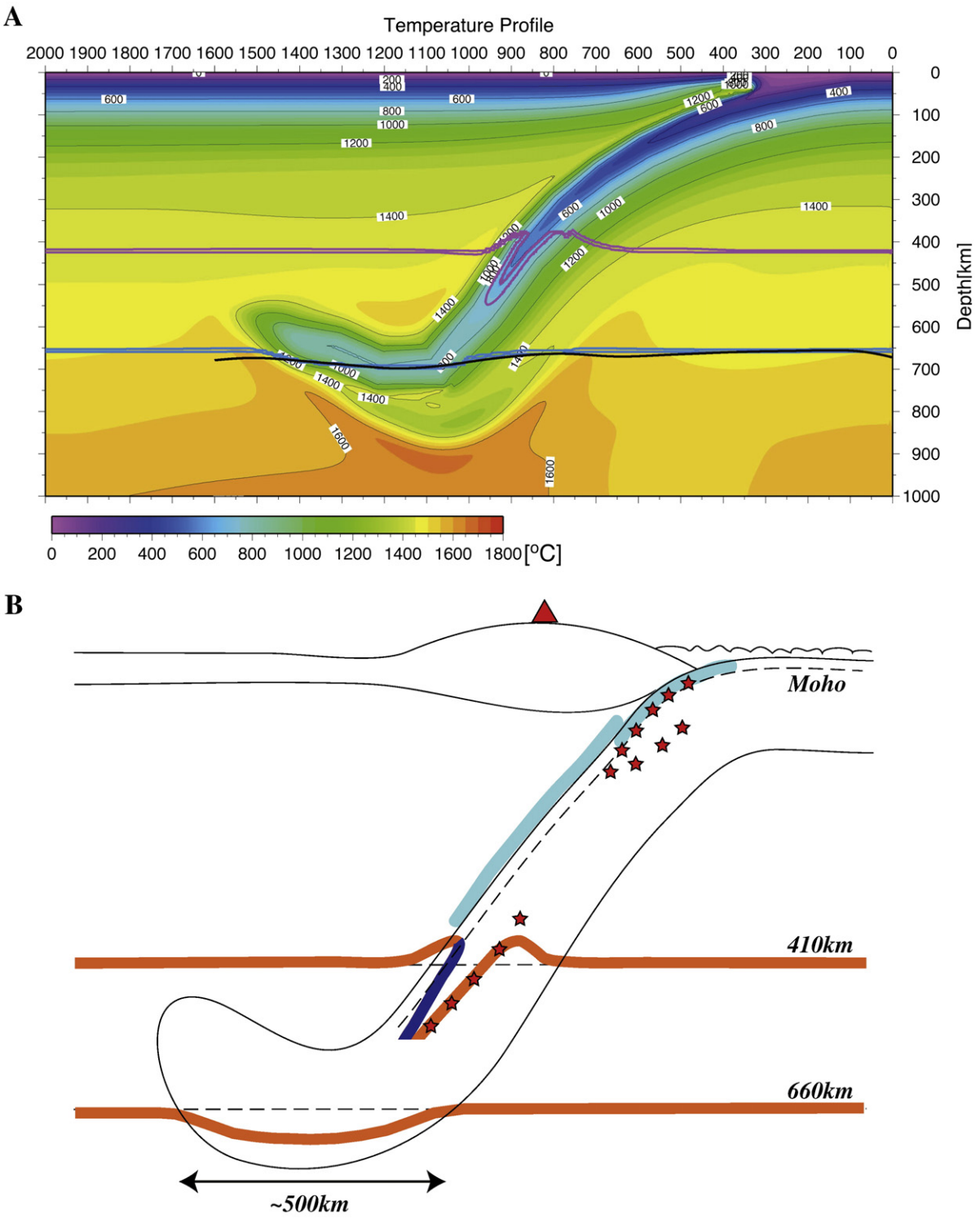

Fig. 10. (A) A similar figure to Fig. 7B but the kinetics of the 660 km-phase transformation is also modeled. The slab in the mantle transition zone is assumed to be slightly deeper than that in Fig. 7B, and the Clapeyron slope is chosen to be −1.3 MPa/K. The black line denotes the location of the 660 km discontinuity imaged in the receiver function analysis (Fig. 1). Note that the observed depression of 660 km-discontinuity is well reproduced. (B) A schematic figure summarizing results of this research. Thick orange and/or blue lines denote imaged 410 km- and 660 km-discontinuities. Colors correspond to those in the reflectivity images. Light-blue lines indicate the inferred pathway of water transported into the deep mantle. Red star symbols correspond to earthquakes occurring within the subducting slab. A red triangle denotes the location of volcanoes in the island-arc.

HK thanks T. Tonegawa for discussion to share the interpretation of images and C. Bina for providing the figure. This research was conducted as a part of the Stagnant Slab Project funded by the Ministry of Education, Culture, Sports, Science and Technology of Japan, and is partly supported by KAKENHI 19104011.

References

Abers, G.A., 2000. Hydrated subducted crust at 100–250 km depth. Earth Planet. Sci. Lett. 176, 323–330.
Ammon, C.J., 1991. The isolation of receiver effects from teleseismic *P* waveforms. Bull. Seismol. Soc. Am. 81, 2504–2510.

Bina, C.R., Helffrich, G., 1994. Phase transition Clapeyron slopes and transition zone seismic discontinuity topography. J. Geophys. Res. 99, 15853–15860.
Bina, C.R., Kawakatsu, H., 2010. Buoyancy, bending, and seismic visibility in deep slab stagnation. Phys. Earth Planet. Inter. 183, 330–340.
Bostock, M.G., Hyndman, R.D., Rondenay, S., Peacock, S.M., 2002. An inverted continental Moho and serpentinization of the forearc mantle. Nature 417, 536–538.
Chen, W.-P., Brudzinski, M.R., 2003. Seismic anisotropy in the mantle transition zone beneath Fiji–Tonga. Geophys. Res. Lett. 30, 1682.
Daessler, R., Yuen, D., 1996. The metastable olivine wedge in fast subducting slabs, constraints from thermokinetic coupling. Earth Planet. Sci. Lett. 137, 109–118.
Fei, Y., Van Orman, J., Li, J., van Westrenen, W., Sanloup, C., Minarik, W., Hirose, K., Komabayashi, K., Walter, M., Funakoshi, K., 2004. Experimentally determined postspinel transformation boundary in Mg_2SiO_4 using MgO as an internal pressure standard and its geophysical implications. J. Geophys. Res. 109, 11–24.
Ferris, A., Abers, G.A., Christensen, D.H., Veenstra, E., 2003. High resolution image of the subducted Pacific plate beneath central Alaska, 50–150 km depth. Earth Planet. Sci. Lett. 214, 575–588.
Fukao, Y., Kanjo, K., Nakamura, I., 1978. Deep seismic zone as an upper mantle reflector of body waves. Nature 272, 606–608.
Fukao, Y., Obayashi, M., Nakakuki, T., 2009. Stagnant slab: a review. Annu. Rev. Earth Planet. Sci. 37, 19–46.
Gudmundsson, O., Sambridge, M.J., 1998. A regionalized upper mantle (RUM) seismic model. J. Geophys. Res. 103, 7121–7136.
Helffrich, G.R., Stein, S., 1993. Study of the structure of the slab–mantle interface using reflected and converted seismic waves. Geophys. J. Int. 115, 14–40.
Hosoya, T., Kubo, T., Ohtani, E., Sano, A., Funakoshi, K., 2005. Water controls the fields of metastable olivine in cold subducting slabs. Geophys. Res. Lett. 32, L17305.
Iidaka, T., Suetsugu, D., 1992. Seismological evidence for metastable olivine inside a subducting slab. Nature 356, 593–595.
Iwamori, H., 2007. Transportation of H_2O beneath the Japan arcs and its implications for global water circulation. Chem. Geol. 239, 182–198.
Iwamori, H., Albaréde, F., 2008. The decoupled isotopic record of ridge and subduction zone processes in oceanic basalts by independent component analysis. Geochem. Geophys. Geosyst. 9, Q04033.
Jiang, G., Zhao, D., Zhang, G., 2008. Seismic evidence for a metastable olivine wedge in the subducting Pacific slab under Japan Sea. Earth Planet. Sci. Lett. 270, 300–307.
Kaneshima, S., Okamoto, T., Takenaka, H., 2007. Evidence for a metastable olivine wedge inside the subducted Mariana slab. Earth Planet. Sci. Lett. 258, 219–227.
Karato, S., 2003. Inside the subduction factory: Geophys. Monogr., 138. AGU, Washington, DC, pp. 135–152.
Katsura, T., Yamada, H., Shinmei, T., Kubo, A., Ono, S., Kanzaki, M., Yoneda, A., Walter, M.J., Ito, E., Urakawa, S., Funakosh, K., Utsumi, W., 2003. Post–spinel transition in Mg_2SiO_4 determined by high P–T in situ X-ray diffraction. Phys. Earth Planet. Inter. 136, 11–24.
Kawakatsu, H., 2008. Sharp top and bottom boundaries of subducting Pacific plate observed via vectorial receiver function analysis for a dipping interface. Japan Geoscience Union Meeting, Abstract I212–002.
Kawakatsu, H., Kumar, P., Takei, Y., Shinohara, M., Kanazawa, T., Araki, E., Suyehiro, K., 2009. Seismic evidence for sharp lithosphere–asthenosphere boundaries of oceanic plates. Science 324, 499–502.
Kawakatsu, H., Watada, S., 2007. Seismic evidence for deep-water transportation in the mantle. Science 316, 1468–1471.
Kelemen, P.B., Hirth, G., 2007. A periodic shear-heating mechanism for intermediate-depth earthquakes in the mantle. Nature 446, 787–790.
Kennett, B.L.N., Engdahl, E.R., 1991. Travel times for global earthquake location and phase identification. Geophys. J. Int. 105, 429–465.
Kubo, T., Kaneshima, S., Torii, Y., Yoshioka, S., 2009. Seismological and experimental constraints on metastable phase transformations and rheology of the Mariana slab. Earth Planet. Sci. Lett. 287, 12–23.
Kubo, T., Ohtani, E., Kato, T., Urakawa, S., Suzuki, A., Kanbe, Y., Funakoshi, K., Utsumi, W., Kikegawa, T., Fujino, K., 2002. Mechanisms and kinetics of the post–spinel transformation in Mg_2SiO_4. Phys. Earth Planet. Inter. 129, 153–171.
Langston, C.A., 1979. Structure under Mount Rainier, Washington, inferred from teleseismic body waves. J. Geophys. Res. 84, 4749–4762.
Li, X., Sobolev, S.V., Kind, R., Yuan, X., Estabrook, C., 2000. A detailed receiver function image of the upper mantle discontinuities in the Japan subduction zone. Earth Planet. Sci. Lett. 183, 527–541.
Marton, F.C., Shankland, T.J., Rubie, D.C., Xu, Y., 2005. Effects of variable thermal conductivity on the mineralogy of subducting slabs and implications for mechanisms of deep earthquakes. Phys. Earth Planet. Inter. 149, 53–64.
Maruyama, S., Okamoto, K., 2007. Water transportation from the subducting slab into the mantle transition zone. Gondwana Res. 11, 148–165.
Matsubara, M., Obara, K., Kasahara, K., 2008. Three-dimensional P-and S-wave velocity structures beneath the Japan Is lands obtained by high-density seismic stations by seismic tomography. Tectonophysics 454, 86–103.
Niu, F., Levander, A., Ham, S., Obayashi, M., 2005. Mapping the subducting Pacific slab beneath southwest Japan with Hi-net receiver functions. Earth Planet. Sci. Lett. 239, 9–17.
Obayashi, M., Yoshimitsu, J., Fukao, Y., 2009. Tearing of stagnant slab. Science 324, 1173–1175.
Okada, H., 1979. New evidence of the discontinuous structure of the descending lithosphere as revealed by S_cS_p phase. J. Phys. Earth 27 (Suppl), S53–S63.
Peacock, S., 2001. Are the lower planes of double seismic zones caused by serpentine dehydration in subducting oceanic mantle? Geology 29, 299–302.
Ramesh, D.S., Kawakatsu, H., Watada, S., Yuan, X., 2005. Receiver function images of the central Chugoku region in the Japanese islands using Hinet data. Earth Planet. Space 57, 271–280.
Revenaugh, J., Sipkin, S.S., 1994. Mantle discontinuity structure beneath China. J. Geophys. Res. 99, 21911–21927.
Reynard, B., Nakajima, J., Kawakatsu, H., 2010. Earthquakes and plastic deformation of anhydrous slab mantle in double Wadati–Benioff zones. Geophys. Res. Lett. 37, L24309.
Rubie, D., Ross, C., 1994. Kinetics of olivine–spinel transformation in subducting lithosphere: experimental constrains and implications for deep slab processes. Phys. Earth Planet. Inter. 86, 223–241.
Schaeffer, A.J., Bostock, M.G., 2010. A low-velocity zone atop the transition zone in northwestern Canada. J. Geophys. Res. 115, B06302.
Shiomi, K., Sato, H., Obara, K., Ohtake, M., 2004. Configuration of subducting Philippine Sea plate beneath southwest Japan revealed from receiver function analysis based on the multivariate autoregressive model. J. Geophys. Res. 109, B04308. doi:10.1029/2003JB002774.
Sung, C.M., Burns, R.G., 1976. Kinetics of high pressure phase transformations: implications to the evolution of olivine–spinel transition in the downgoing lithosphere and its consequences on the dynamics of the mantle. Tectonophysics 31, 1–32.
Tauzin, B., Debayle, E., Wittlinger, G., 2010. Seismic evidence for a global low-velocity layer within the Earth's upper mantle. Nat. Geosci. 3, 718–721.
Tonegawa, T., Hirahara, K., Shibutani, T., Iwamori, H., Kanamori, H., Shiomi, K., 2008. Water flow to the mantle transition zone inferred from a receiver function image of the Pacific slab. Earth Planet. Sci. Lett. 274, 346–354.
Tono, Y., Fukao, Y., Kunugi, T., Tsuboi, S., 2009. Seismic anisotropy of the Pacific slab and mantle wedge beneath the Japanese islands. J. Geophys. Res. 114, B07307.
Tsuji, Y., Nakajima, J., Hasegawa, A., 2008. Tomographic evidence for hydrated oceanic crust of the Pacific slab beneath northeastern Japan: implications for water transportation in subduction zones. Geophys. Res. Lett. 35, L14308.
Vinnik, L.P., 1977. Detection of waves converted from P to SV in the mantle. Phys. Earth Planet. Inter. 15, 39–45.
Wiens, D.A., McGuire, J.J., Shore, P.J., 1993. Evidence for transformational faulting from a deep double seismic zone in Tonga. Nature 364, 790–793.
Yoshioka, S., Torii, Y., Kubo, T., Riedel, M.R., 2008. 2D temperature model in deep slabs incorporating kinetics of the 410-km and 660-km phase transformations — application to the Mariana slab. The 7th General Assembly of Asian Seismological Commission and the 2008 fall meeting of Seismological Society of Japan, D22-08.
Yoshioka, S., Torii, Y., Kubo, T., Riedel, M. R., in preparation. A 2-D slab subduction model incorporating kinetics of phase transformation — application to the Mariana slab.
Yuan, X., Sobolev, S.V., Kind, R., Oncken, O.G., Bock, G.A., Schurr, B., Graeber, F., et al., 2000. Subduction and collision processes in the Central Andes constrained by converted seismic phases. Nature 408, 958–961.